Screened Copy-Time Transport at Cosmic Dawn: A Microscopic Onsager Mechanism for Early Galaxy Compaction and Black-Hole Seed Growth

Mohamed Sacha
Independent Researcher; corresponding author: www.sachamed@gmail.com
Theoretical and methodological manuscript, April 2026

Abstract. This paper formulates screened copy-time transport as a projected nonequilibrium mechanism for baryonic supply at cosmic dawn. The construction starts from ordinary baryon-electron-photon microphysics and defines a receiver algebra of outgoing records. A Mori-Fisher projection removes all record information already represented in standard radiation hydrodynamics: mass, momentum, gas energy, radiation groups, chemistry and opacities. The remaining scalar is not an adjustable potential but the logarithmic excess of the structural Fisher-information rate,

$$\psi = \log\left(\frac{\dot{\mathcal{I}}_Q^{\mathrm{raw}}}{\dot{\mathcal{I}}_Q^{\parallel}}\right) = \log(1 + \dot{\mathcal{I}}_Q^{\perp}/\dot{\mathcal{I}}_Q^{\parallel}),$$

where the denominator is fixed by the projected standard channel. This normalization eliminates the former arbitrary time scale. The residual receiver modifies the coarse-grained measure by a Radon-Nikodym factor whose entropy density is $q_Q n_b \psi$. Its variational derivative gives the thermodynamic force $q_Q \nabla\psi$, so Onsager theory fixes the cross coefficient,

$$L_{B\psi}^{(\ell)} = q_Q L_{BB}^{(\ell)} = q_Q n_b D_B^{(\ell)}.$$

The coefficient has exact Green-Kubo/Mori and projected-Boltzmann forms. Molecular diffusion is shown by dimensional analysis to be far below the required mobility for galaxy-scale compaction; the relevant astrophysical coefficient is the filtered Kubo mobility of resolved, cooled, turbulent gas. The paper derives the quadratic structural coefficient A_2 for one-body, two-body and three-body record channels, supplies power inequalities for dynamical relevance, gives a conservative radiation-hydrodynamic insertion operator, defines the observable selection test, and states discriminating predictions.

Keywords: nonequilibrium transport; Onsager reciprocity; Mori projection; Fisher information; radiation hydrodynamics; cosmic dawn; black-hole seeds; JWST.

Contents

1 Introduction 1

2 Microscopic receiver and projection 2

3 Projection theorem for the quadratic structural coefficient 3

4 Coarse-grained entropy and Onsager coefficient 6

5 Microscopic mobility and the molecular null result 7

6 Filtered Kubo mobility and power criteria 7

7 Linear cosmological screening 8

8 Receiver window **10**

9 Conservative radiation-hydrodynamic operator **10**

10 Black-hole feeding and observables **12**

11 Halo catalogues, feeding histories and forward-modelled observables **13**

12 Predictions and discriminants **14**

13 Numerical validation protocol **15**

14 Code and reproducibility **17**

15 Conclusion **17**

1 Introduction

The observational problem is not merely that luminous galaxies exist at high redshift; it is that compact stellar systems, obscured active nuclei and large inferred black-hole masses appear within a limited cosmic time. Spectroscopic confirmation of JADES-GS-z14-0 at $z \simeq 14.32$ demonstrates that luminous galaxies were present approximately 300 Myr after the Big Bang [16, 17]. UHZ1 has been interpreted as an X-ray source consistent with a heavy-seed origin [18]. CAPERS-LRD-z9 is a broad-line active nucleus at $z = 9.288$, with a canonical virial mass near $10^{7.58} M_\odot$ and large systematic uncertainty [19]. These observations motivate an additional supply mechanism only if it is conservative, screened from primary linear cosmology, not already contained in ordinary radiation hydrodynamics, and testable in matched simulations.

The analysis is formulated as a projected transport construction together with a validation protocol. Gravity, baryon number conservation and the standard accretion equation are kept fixed. The additional element is a residual structural record, defined only after the response already represented in radiation hydrodynamics has been projected out. This residual record defines an entropic scalar ψ. When both $\nabla\psi$ and the filtered baryonic mobility are sufficiently large in cooled nonlinear gas, the associated Onsager current modifies the central gas supply; otherwise the transport channel is dynamically irrelevant by the power inequalities derived below.

2 Microscopic receiver and projection

On subhorizon cosmic-dawn scales the microscopic Hamiltonian can be written schematically as

$$H = H_{be\gamma} + H_{\mathrm{Th}} + H_{\mathrm{bf}} + H_{\mathrm{ff}} + H_{\mathrm{line}} + H_{\mathrm{chem}} + H_{\mathrm{grav}}, \tag{1}$$

where the interaction terms denote Thomson scattering, bound-free and free-free processes, line emission, nonequilibrium chemistry and self-gravity. The receiver algebra $\mathcal{A}_{\mathrm{rec}}$ is generated by stable outgoing records: photon occupation operators at cell or null boundaries, escaped line photons, scattering histories, and environmental states that remain correlated with the baryonic configuration over a coarse-graining interval.

Let Y be receiver data produced in a spacetime cell and let Q be a baryonic coarse variable. The score is

$$s_Q(Y) = \partial_Q \log p(Y \mid Q). \tag{2}$$

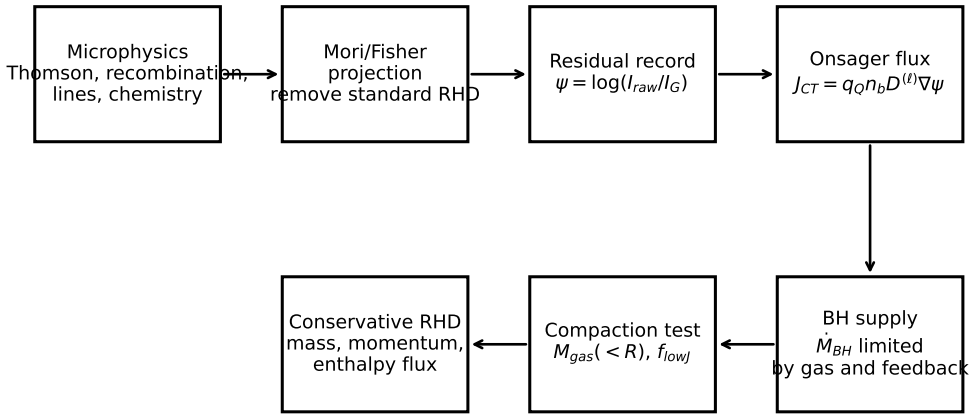

Figure 1: Logical architecture of screened copy-time transport. Ordinary microphysics produces records; the Mori-Fisher projection removes the part already represented in standard RHD; the residual Fisher scalar supplies an entropy-gradient force; the resulting Onsager current is inserted as a conservative flux; compaction and black-hole feeding are tested only through matched simulations and identical selection functions.

The raw Fisher-information rate is

$$\dot{\mathcal{I}}_Q^{\rm raw} = \lim_{\Delta t\to 0} \frac{1}{\Delta t} \left\langle s_Q(Y)^2 \right\rangle . \tag{3}$$

For independent microscopic record channels r,

$$\dot{\mathcal{I}}_Q^{\rm raw} = \sum_r \int {\rm d}\Pi_r \, \dot{N}_r(\Pi_r) \left\langle [\partial_Q \log p_r(Y \mid Q, \Pi_r)]^2 \right\rangle . \tag{4}$$

For a Poisson channel with rate $R_r(Q)$,

$$\dot{\mathcal{I}}_{Q,r}^{\rm raw} = \frac{(\partial_Q R_r)^2}{R_r}. \tag{5}$$

Equation (5) makes the record rate calculable from cross sections and emissivity kernels. It also identifies the subtraction required for consistency: unprojected record rates contain ordinary one-point density responses already represented by radiation forces, cooling and opacities. The copy-time channel is therefore defined only on the Fisher-orthogonal residual.

Definition 1 (Standard RHD score space)**.** *Let $\mathcal{G}$ be the score space generated by all slow variables explicitly evolved by the baseline radiation-hydrodynamic solver: baryon number, momentum, gas energy, radiation energy density and flux in each photon group, chemical and ionization abundances, metal mass, opacities, emissivities and any subgrid feedback state used in both baseline and copy-time runs. With Fisher inner product $(a,b)_F = \langle ab \rangle$, define $\mathcal{P}_\mathcal{G}$ as the orthogonal projector onto $\mathcal{G}$.*

The raw score is decomposed as

$$s_Q = s_Q^{\parallel} + s_Q^{\perp}, \qquad s_Q^{\parallel} = \mathcal{P}_{\mathcal{G}} s_Q, \qquad s_Q^{\perp} = (1 - \mathcal{P}_{\mathcal{G}}) s_Q. \tag{6}$$

The associated Fisher rates are

$$\dot{\mathcal{I}}_Q^{\parallel} = \lim_{\Delta t \to 0} \frac{1}{\Delta t} \langle (s_Q^{\parallel})^2 \rangle, \qquad \dot{\mathcal{I}}_Q^{\perp} = \lim_{\Delta t \to 0} \frac{1}{\Delta t} \langle (s_Q^{\perp})^2 \rangle. \tag{7}$$

The copy-time scalar is then defined by the dimensionless excess ratio

$$\boxed{\psi = \log \left(\frac{\dot{\mathcal{I}}_Q^{\mathrm{raw}}}{\dot{\mathcal{I}}_Q^{\parallel}} \right) = \log \left(1 + \frac{\dot{\mathcal{I}}_Q^{\perp}}{\dot{\mathcal{I}}_Q^{\parallel}} \right).} \tag{8}$$

This definition is preferable to $\psi = \log(\tau_0 \dot{\mathcal{I}}^{\perp})$. It introduces no arbitrary clock. If the residual record channel vanishes, $\psi = 0$. If the residual channel is spatially homogeneous, $\nabla \psi = 0$ and no transport follows.

3 Projection theorem for the quadratic structural coefficient

The amplitude controlling $\nabla \psi$ is the residual structural coefficient A_2. It must be computed from microscopic channel rates and from resolved or subgrid clumping statistics. It is not a fitted constant.

Consider a cell of volume V_ℓ. Let a record channel have local reaction order p,

$$R_r = K_r(T, \boldsymbol{x}) \int_{V_\ell} \prod_{a=1}^{p} n_a(\mathbf{x}) \, \mathrm{d}^3 x, \tag{9}$$

where K_r is a cross-section, recombination, excitation, chemistry or emissivity kernel. Write

$$n_a(\mathbf{x}) = \bar{n}_a [1 + \delta_a(\mathbf{x})], \qquad \langle \delta_a \rangle_\ell = 0. \tag{10}$$

The variables $\bar{n}_a, T, \boldsymbol{x}$ belong to $\mathcal{G}$. The residual structural invariants begin with the cell covariances

$$C_{ab,\ell} = \langle \delta_a \delta_b \rangle_\ell. \tag{11}$$

For a smooth field in a Cartesian finite-volume cell,

$$C_{ab,\ell} = \frac{\ell^2}{12} \nabla \log n_a \cdot \nabla \log n_b + O(\ell^4 \nabla^4), \tag{12}$$

so the leading resolved estimate is fixed by the state of the simulation. A subgrid clumping model may add a term, but then it must be used identically in baseline and copy-time runs and calibrated independently of the high-redshift compact-source outcome.

Theorem 1 (Poisson projection coefficient)**.** *For a p-body Poisson record channel whose one-point response is projected into $\mathcal{G}$, the leading residual Fisher rate for a long-mode amplitude δ_L is*

$$\dot{\mathcal{I}}_{\delta_L, r}^{\perp} = A_{2,r} \delta_L^2 + O(\delta_L^3), \qquad A_{2,r} = [p(p-1)\chi_{r,2}]^2 \, R_{r0}, \tag{13}$$

where $R_{r0} = K_r V_\ell \prod_a \bar{n}_a$ and $\chi_{r,2} = \partial C_{r,\ell} / \partial (\delta_L^2)|_0$ is the clumping-response coefficient measured from the resolved field or from an independently calibrated closure. For $p = 1$, $A_{2,r} = 0$.

Proof. Expanding Eq. (9) at fixed cell means gives

$$R_r = R_{r0}\left[1 + \sum_{a<b} C_{ab,\ell} + O(\delta^3)\right]. \tag{14}$$

For equal long-mode response this may be written as

$$R_r = R_{r0}\left[1 + \frac{p(p-1)}{2}\chi_{r,2}\delta_L^2 + O(\delta_L^3)\right]. \tag{15}$$

The linear response has already been removed by $\mathcal{P}_{\mathcal{G}}$. Hence

$$\partial_{\delta_L} R_r^{\perp} = p(p-1)R_{r0}\chi_{r,2}\delta_L + O(\delta_L^2). \tag{16}$$

Substitution into the Poisson Fisher identity (5) and evaluation of the denominator at R_{r0} yields Eq. (13). The factor $p(p-1)$ vanishes for a one-body channel, proving the Thomson and one-point opacity null result after projection. □

The channel-level consequences are explicit:

$$A_{2,\mathrm{Th}} = 0, \tag{17}$$

$$A_{2,\mathrm{bf}} = 0 \quad \text{for one-point opacity already in RHD}, \tag{18}$$

$$\frac{A_{2,\mathrm{rec}}}{V_\ell} = 4\chi_{ep,2}^2 \alpha_B(T) n_e n_p, \tag{19}$$

$$\frac{A_{2,\mathrm{Ly}\alpha}}{V_\ell} = 4\chi_{ep,2}^2 f_\alpha \beta_{\mathrm{esc}} \alpha_B(T) n_e n_p, \tag{20}$$

$$\frac{A_{2,\mathrm{ff}}}{V_\ell} = 4\chi_{ei,2}^2 K_{\mathrm{ff}}(T,\nu) n_e n_i, \tag{21}$$

$$\frac{A_{2,\mathrm{line}}}{V_\ell} = 4\chi_{eX,2}^2 q_{ul}(T) n_e n_X, \tag{22}$$

$$\frac{A_{2,3\mathrm{body\ H_2}}}{V_\ell} = 36\chi_{H,2}^2 k_3(T) n_H^3. \tag{23}$$

Here α_B is the case-B recombination coefficient, f_α the Lyα branching factor, β_{esc} an escape probability computed by the radiative-transfer solver, K_{ff} a photon-count free-free kernel, q_{ul} a collisional excitation rate and k_3 a three-body molecular-hydrogen formation rate. Every factor is either a microphysical rate table, a radiative-transfer quantity, or a structural covariance determined before comparison with high-redshift source statistics.

With the decomposition $\dot{\mathcal{I}}^{\mathrm{raw}} = \dot{\mathcal{I}}^{\parallel} + \dot{\mathcal{I}}^{\perp}$, the leading nonlinear scalar is

$$\psi = \log\left[1 + \frac{\sum_r A_{2,r}\delta_L^2 + O(\delta_L^3)}{\dot{\mathcal{I}}^{\parallel}}\right]. \tag{24}$$

Hence A_2 is the quantity that determines whether the gradients of ψ can become astrophysically important in collapsed gas. It is no longer an open symbol: Eqs. (19)–(23) give its channel-level form.

Table 1: Projected record channels and quadratic coefficients. R_0 is the zero-order rate in the cell. The normalized coefficient assumes $\chi_{r,2} = 1$; production calculations use the measured $\chi_{r,2}$.

Channel	Rate kernel	A_2/R_0
Thomson one-point	$\sigma_T c n_e n_\gamma$	0
Photoionization opacity	$c n_\gamma n_{\rm HI} \sigma_\nu$	0
Case-B recombination	$\alpha_B(T) n_e n_p$	$4\chi^2_{ep,2}$
Recombination Lyα	$f_\alpha \beta_{\rm esc} \alpha_B n_e n_p$	$4\chi^2_{ep,2}$
Free-free photons	$K_{\rm ff} n_e n_i$	$4\chi^2_{ei,2}$
Collisional line	$q_{ul} n_e n_X$	$4\chi^2_{eX,2}$
Three-body H_2	$k_3 n_H^3$	$36\chi^2_{H,2}$

4 Coarse-grained entropy and Onsager coefficient

The residual receiver changes the coarse-grained measure, not the fundamental Hamiltonian. Let Γ_0 be the standard hydrodynamic measure after tracing over fast variables whose mean effects are already in $\mathcal{G}$. The structural receiver contributes the Radon-Nikodym factor

$$\frac{\mathrm{d}\Gamma_{\rm cg}}{\mathrm{d}\Gamma_0} = \exp\left[\int q_Q n_b(x)\psi(x)\,\mathrm{d}^3x\right]. \tag{25}$$

For the baryon-number copy coordinate, $q_Q = 1$ by normalization of the conserved unit. If a different conserved scalar is copied, q_Q changes by redefining Q; it is not a continuous population-fit parameter.

The entropy functional is

$$S[n_b, e, \psi] = \int \mathrm{d}^3x\ [s_0(n_b, e) + q_Q n_b \psi]\,, \tag{26}$$

so at fixed energy density

$$\frac{\delta S}{\delta n_b} = -\frac{\mu_B}{T} + q_Q\psi. \tag{27}$$

The baryonic thermodynamic force in a relativistic notation is

$$\mathbb{X}^\mu_B = \Delta^{\mu\nu}\nabla_\nu\left(\frac{\delta S}{\delta n_b}\right) = -\Delta^{\mu\nu}\nabla_\nu\left(\frac{\mu_B}{T}\right) + q_Q\Delta^{\mu\nu}\nabla_\nu\psi. \tag{28}$$

Theorem 2 (No independent baryon-copy Onsager coefficient)**.** *At coarse-graining scale ℓ,*

$$\boxed{L^{(\ell)}_{B\psi} = q_Q L^{(\ell)}_{BB} = q_Q n_b D^{(\ell)}_B.} \tag{29}$$

Proof. The entropy production in the single relative baryon channel is

$$\nabla_\mu s^\mu = \nu^\mu_B \mathbb{X}_{B\mu}. \tag{30}$$

The isotropic Onsager law is $\nu^\mu_B = L^{(\ell)}_{BB}\mathbb{X}^\mu_B$, with $L^{(\ell)}_{BB} \geq 0$. Substitution of Eq. (28) gives

$$\nu^\mu_B = L^{(\ell)}_{BB} X^\mu_B + q_Q L^{(\ell)}_{BB} X^\mu_\psi, \tag{31}$$

where $X^\mu_B = -\Delta^{\mu\nu}\nabla_\nu(\mu_B/T)$ and $X^\mu_\psi = \Delta^{\mu\nu}\nabla_\nu\psi$. Comparison with a two-force notation gives Eq. (29). Any different cross coefficient would correspond to an additional entropy term not present in Eq. (26). □

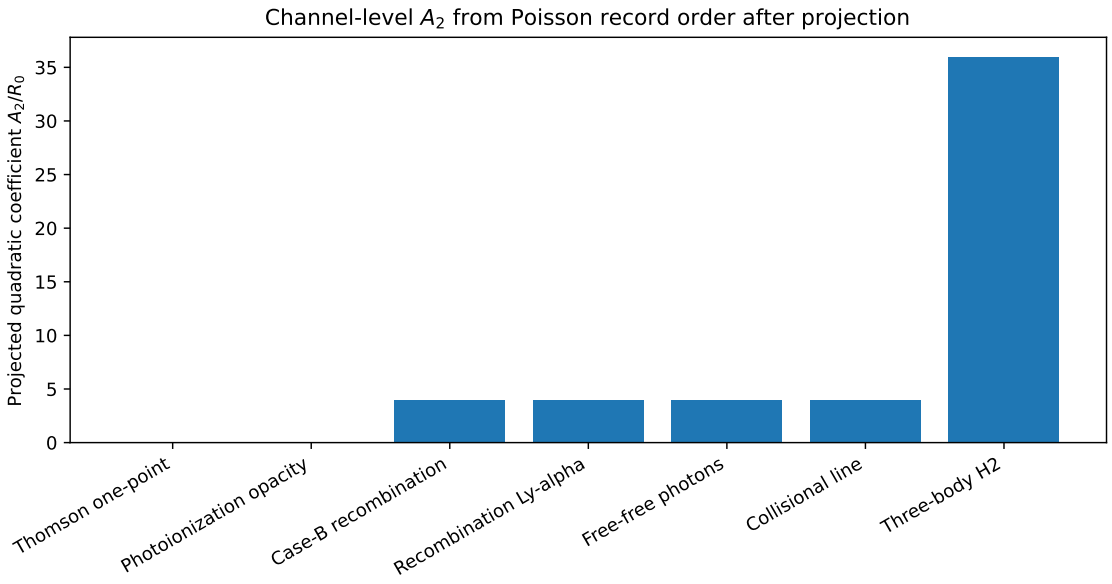

Figure 2: Normalized structural coefficient produced by the projection theorem. One-body channels vanish after standard RHD projection. Two-body and three-body channels survive only through measured clumping/covariance response; their absolute amplitudes are fixed by microscopic rate kernels and local gas state.

The corresponding two-force matrix is rank one,

$$\mathbf{L} = L_{BB}^{(\ell)} \begin{pmatrix} 1 & q_Q \\ q_Q & q_Q^2 \end{pmatrix}, \qquad \mathbf{a}^T \mathbf{L} \mathbf{a} = L_{BB}^{(\ell)} (a_1 + q_Q a_2)^2 \geq 0. \tag{32}$$

Additional receiver relaxation variables may add positive diagonal blocks, but they do not alter the cross coefficient that couples to the baryon current.

5 Microscopic mobility and the molecular null result

The exact Kubo-Mori expression for the baryonic mobility is

$$L_{BB}^{(\ell)} = \frac{1}{3T} \int_0^\infty \mathrm{d}t \int_{|\mathbf{x}|<\ell} \mathrm{d}^3 x \, \left\langle J_B^i(t,\mathbf{x}) J_B^i(0,\mathbf{0}) \right\rangle_{\perp,\ell}, \tag{33}$$

where zero modes and the standard RHD score space are projected out. Thus

$$\boxed{L_{B\psi}^{(\ell)} = \frac{q_Q}{3T} \int_0^\infty \mathrm{d}t \int_{|\mathbf{x}|<\ell} \mathrm{d}^3 x \, \left\langle J_B^i(t,\mathbf{x}) J_B^i(0,\mathbf{0}) \right\rangle_{\perp,\ell}.} \tag{34}$$

In kinetic theory this becomes

$$L_{B\psi}^{\mathrm{mol}} = \frac{q_Q}{3T} \sum_s \left(\mathcal{V}_{B,s}^i, \mathcal{C}_{s,\perp}^{-1} \mathcal{V}_{B,s}^i \right)_s, \tag{35}$$

where $\mathcal{C}_\perp^{-1}$ is the inverse of the linearized collision operator on the dissipative subspace. A relaxation closure gives

$$D_B^{\mathrm{mol}} = \frac{k_\mathrm{B} T}{m_B \nu_{\mathrm{tr}}}, \qquad L_{B\psi}^{\mathrm{mol}} = q_Q n_b D_B^{\mathrm{mol}}, \tag{36}$$

with

$$\nu_{\rm tr} = \sum_a n_a \langle \sigma_{Ba}^{\rm tr} v_{Ba} \rangle + \nu_{\gamma b} + \nu_{\rm Coul} + \nu_{\rm mol} + \nu_{\rm dust} + \cdots , \tag{37}$$

including, for photon drag,

$$\nu_{\gamma b} = \frac{4\rho_\gamma}{3\rho_b} n_e \sigma_T c. \tag{38}$$

Proposition 1 (Molecular diffusion cannot compact a galaxy)**.** *For* $D_B^{\rm mol} \sim 10^9$–$10^{11}\,{\rm m^2\,s^{-1}}$*, the diffusion time over* $L = 10$–100 *pc is*

$$t_{\rm diff}^{\rm mol} = \frac{L^2}{D_B^{\rm mol}} \simeq 3 \times 10^{16}\,{\rm yr} \left(\frac{L}{10\,{\rm pc}}\right)^2 \left(\frac{10^{11}\,{\rm m^2\,s^{-1}}}{D_B^{\rm mol}}\right). \tag{39}$$

This exceeds any cosmic-dawn formation time by many orders of magnitude. Molecular diffusion is therefore not the astrophysical channel.

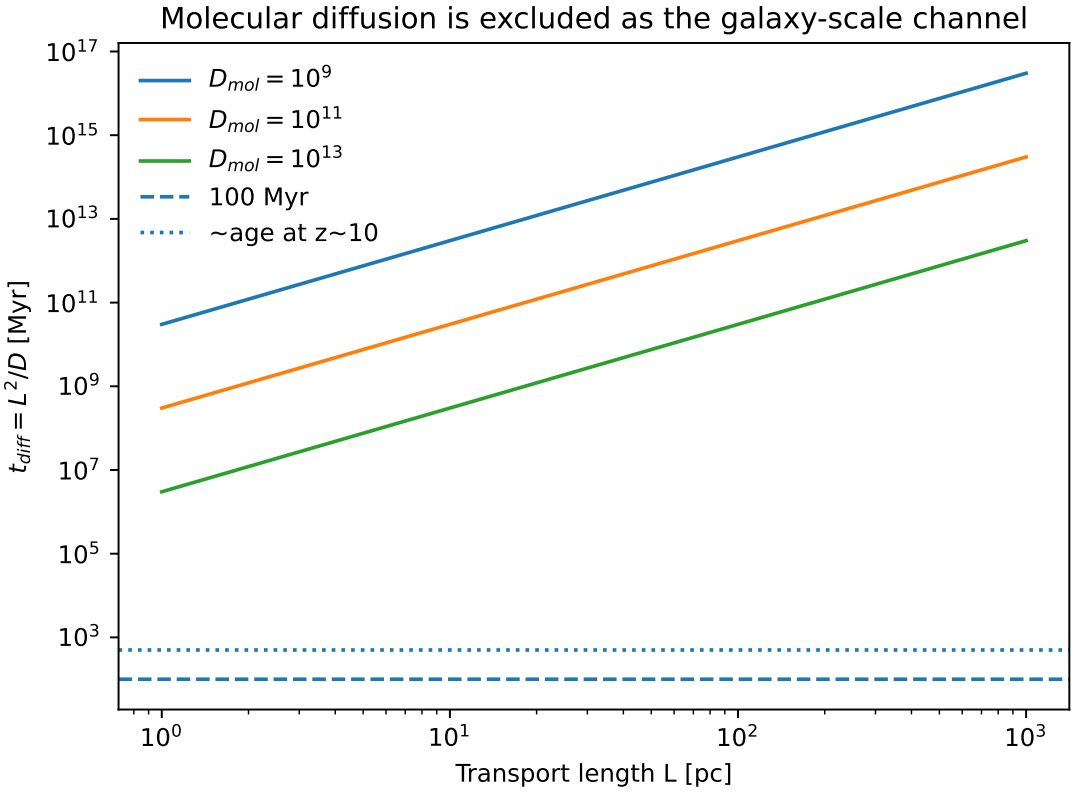

Figure 3: Molecular diffusion is far below the required mobility for 10–100 pc compaction. The calculation eliminates the molecular coefficient as the galaxy-scale channel and identifies the filtered Kubo mobility of resolved gas as the relevant transport coefficient.

6 Filtered Kubo mobility and power criteria

The relevant coefficient in a finite-resolution radiation-hydrodynamic calculation is the filtered Green-Kubo mobility

$$D_B^{(\ell)} = \frac{1}{3}\int_0^\infty \mathrm{d}t\, \langle \delta\mathbf{u}_\ell(t)\cdot\delta\mathbf{u}_\ell(0)\rangle_\perp, \tag{40}$$

where $\delta\mathbf{u}_\ell$ is the baryonic velocity fluctuation in a cell after subtracting the resolved advective flow and projecting out ordinary RHD variables. If the autocorrelation is locally exponential,

$$D_B^{(\ell)} = \frac{1}{3}\sigma_\ell^2\tau_\ell, \qquad \tau_\ell \le \frac{\ell}{\sigma_\ell}. \tag{41}$$

The quantities σ_ℓ and τ_ℓ are measured from the simulation state. They are determined from the local simulation state before the observable comparison.

Let $L_\psi = |\nabla\psi|^{-1}$ be the coherence length of the copy-time scalar and let L be the target inflow scale. The drift speed and drift time are

$$v_{\mathrm{CT}} \simeq \frac{D_B^{(\ell)}}{L_\psi}, \qquad t_{\mathrm{drift}} \simeq \frac{LL_\psi}{D_B^{(\ell)}}. \tag{42}$$

The channel is dynamically relevant only if

$$\frac{LL_\psi}{t_{\mathrm{dyn}}} \lesssim D_B^{(\ell)} \lesssim v_{\max}L_\psi, \tag{43}$$

where $v_{\max}$ is at most the resolved sound or turbulent speed. Equation (43) is a necessary consistency condition: if the lower bound exceeds the speed bound, the channel cannot compact gas within the assumed hydrodynamic regime.

Table 2: Operational quantities. None is fitted to the observed compact-source population.

Quantity	Definition	How fixed in production
q_Q	copied baryon-number unit	normalization; $q_Q = 1$
ψ	$\log(\dot{\mathcal{I}}^{\mathrm{raw}}/\dot{\mathcal{I}}^{\parallel})$	channel rates and projection
A_2	Eq. (13)	microphysical kernels and measured clumping
D_B^{mol}	$k_{\mathrm{B}}T/(m_B\nu_{\mathrm{tr}})$	null lower-bound diagnostic
$D_B^{(\ell)}$	Eq. (40)	velocity autocorrelation in RHD
τ_ℓ	decorrelation time	measured; $\le \ell/\sigma_\ell$
L_ψ	$\lvert\nabla\psi\rvert^{-1}$	computed from projected Fisher field

7 Linear cosmological screening

The screened mechanism must not introduce an unconstrained first-order source in the CMB or BAO equations. The projection supplies the necessary condition.

Theorem 3 (Projected primary linear screen)**.** *Assume the FRW reference state is homogeneous and isotropic, and assume $\mathcal{G}$ contains all one-point hydrodynamic, thermochemical and radiation variables with nonzero first-order scalar response. Then the copy-time force has no primary linear scalar source:*

$$\frac{\delta}{\delta\delta(\mathbf{k})}\,\Delta^{\mu\nu}\nabla_\nu\psi\Big|_{\delta=0} = 0. \tag{44}$$

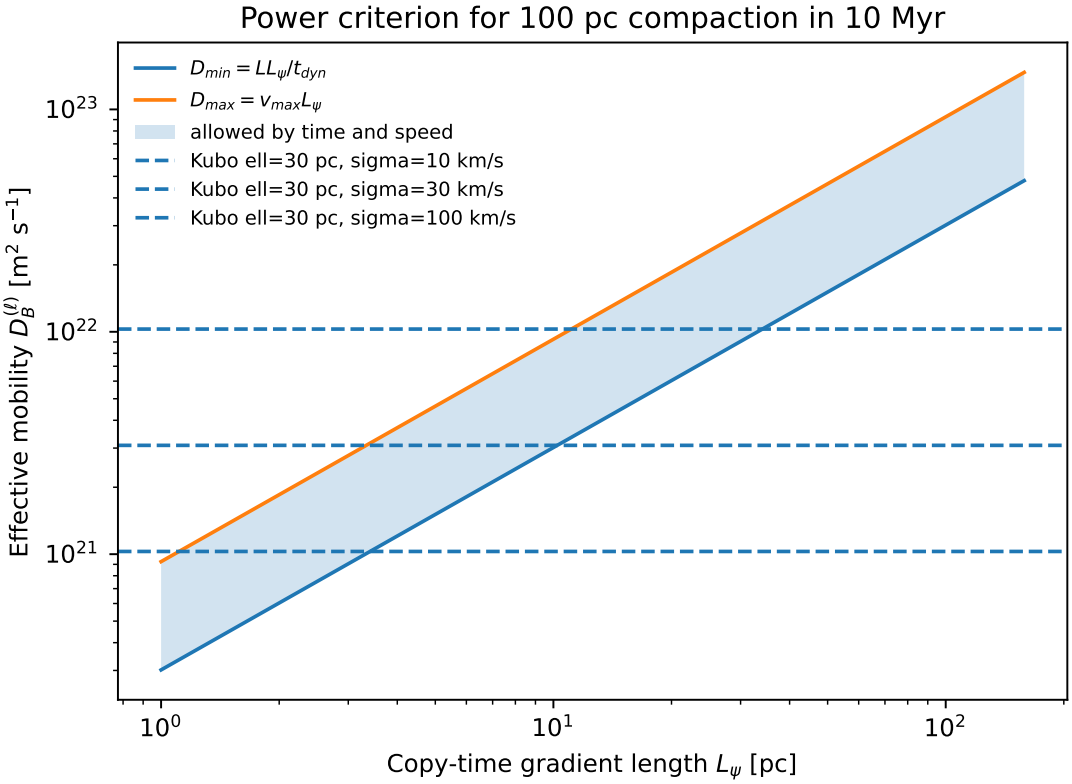

Figure 4: Power criterion for a representative 100 pc compaction problem. The lower curve gives the minimum mobility required to act within a 10 Myr dynamical time; the upper curve imposes $v_{\rm CT} < 30\,{\rm km\,s^{-1}}$. Molecular values are far below the plotted range. Dynamical relevance requires filtered mobilities characteristic of cooled, turbulent gas.

Proof. The raw score can be expanded as

$$s_Q = s_Q^{(0)} + \delta s_Q^{(1)} + \delta^2 s_Q^{(2)} + \cdots . \tag{45}$$

The homogeneous term has no spatial gradient. By hypothesis, the entire first-order scalar score belongs to $\mathcal{G}$, hence $(1-\mathcal{P}_\mathcal{G})s_Q^{(1)} = 0$. The residual Fisher excess therefore begins with the quadratic structural coefficient,

$$\frac{\dot{\mathcal{I}}_Q^\perp}{\dot{\mathcal{I}}_Q^\parallel} = B_2\delta^2 + O(\delta^3), \tag{46}$$

where $B_2 = A_2/\dot{\mathcal{I}}_Q^\parallel$. Thus

$$\psi = \log(1 + B_2\delta^2 + O(\delta^3)) = B_2\delta^2 + O(\delta^3), \tag{47}$$

and $\nabla\psi$ contains no term linear in δ. □

In a formal baryon Euler equation,

$$\theta_b' = -\mathcal{H}\theta_b + c_b^2 k^2\delta_b + R_\gamma(\theta_\gamma - \theta_b) + k^2\Phi + q_{\rm CT}, \tag{48}$$

this means

$$q_{\rm CT}^{(1)} = 0. \tag{49}$$

The leading contribution is nonlinear,

$$q_{\rm CT}^{(2)}(\mathbf{k}, a) = \int \frac{{\rm d}^3 p}{(2\pi)^3} K_{\rm CT}(\mathbf{p}, \mathbf{k}-\mathbf{p}; a)\delta_b(\mathbf{p})\delta_b(\mathbf{k}-\mathbf{p}), \tag{50}$$

with $K_{\rm CT}$ fixed by the projected Fisher rates, the receiver window and the measured mobility. Linear screening is therefore structural, not tuned; nonlinear matter statistics and halo structure remain constraints.

8 Receiver window

A receiver cannot record a homogeneous conserved displacement inside a closed cell, and it cannot resolve structure below the decorrelation length. The finite-band response is

$$W_{\rm rec}(a, k) = \frac{k_{\rm phys}^2}{k_{\rm phys}^2 + k_J^2(a)} \frac{1}{1 + k_{\rm phys}^2 \lambda_{\rm res}^2(a)}, \qquad k_{\rm phys} = \frac{k}{a}, \tag{51}$$

where

$$k_J = \frac{\sqrt{4\pi G \rho_b}}{c_s}, \qquad \lambda_{\rm res} = \sqrt{D_B^{(\ell)} \tau_\ell}. \tag{52}$$

The low-k factor follows from conservation and pressure support; the high-k factor follows from finite receiver resolution. The peak scale is determined by the local gas state and decorrelation length, not fitted to an observed galaxy size.

9 Conservative radiation-hydrodynamic operator

In a single barycentric fluid there is no independent diffusion of total baryon mass. The copy-time current is therefore a filtered relative flux in the coarse-grained equations. It is not a second baryon species and not a source term. Let $\mathbf{u}$ be the resolved advective velocity. The number flux is

$$\partial_t n_b + \nabla \cdot (n_b \mathbf{u} + \mathbf{J}_{\rm CT}) = 0, \tag{53}$$

with Maxwell-Cattaneo completion

$$\tau_\ell (\partial_t + \mathbf{u} \cdot \nabla)\mathbf{J}_{\rm CT} + \mathbf{J}_{\rm CT} = -D_B^{(\ell)} \nabla n_b + q_Q D_B^{(\ell)} n_b \nabla \psi. \tag{54}$$

The entropy production is

$$\sigma_{\rm CT} = \frac{|\mathbf{J}_{\rm CT}|^2}{n_b D_B^{(\ell)}} \geq 0. \tag{55}$$

The mass flux $\mathbf{j}_m = m_b \mathbf{J}_{\rm CT}$ carries momentum and enthalpy:

$$\partial_t \rho_b + \nabla \cdot (\rho_b \mathbf{u} + \mathbf{j}_m) = 0, \tag{56}$$

$$\partial_t (\rho_b \mathbf{u}) + \nabla \cdot (\rho_b \mathbf{u}\mathbf{u} + P\mathbf{I} + \mathbf{u}\mathbf{j}_m) = -\rho_b \nabla \Phi + \mathbf{f}_{\rm rad} + \mathbf{f}_{\rm fb}, \tag{57}$$

$$\partial_t E + \nabla \cdot \left[(E + P)\mathbf{u} + \mathbf{F}_{\rm rad} + h_b \mathbf{J}_{\rm CT} + \frac{1}{2} m_b u^2 \mathbf{J}_{\rm CT} \right] = -\rho_b \mathbf{u} \cdot \nabla \Phi + \dot{E}_{\rm rad} + \dot{E}_{\rm fb}. \tag{58}$$

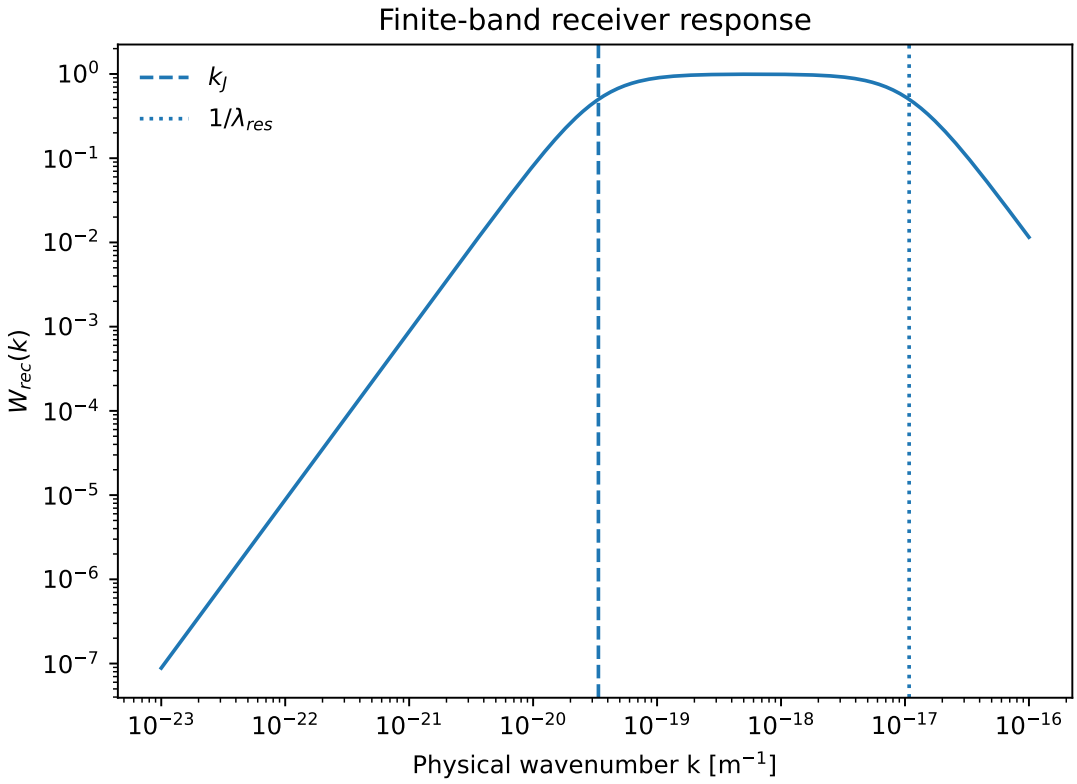

Figure 5: Finite-band receiver response for an illustrative filtered decorrelation length. In production calculations both k_J and λ_{res} are evaluated locally from the simulation state.

Poisson's equation is solved after the density update,

$$\nabla^2\Phi = 4\pi G(\rho_b + \rho_{\mathrm{dm}} + \rho_\star + \rho_{\mathrm{BH}} - \bar{\rho}), \tag{59}$$

so gravity responds to the baryon redistribution. Cooling, nonequilibrium chemistry, star formation and black-hole sink prescriptions are then applied using the updated conservative state. This ordering prevents hidden nonconservation.

For constant $D_B^{(\ell)}$, τ_ℓ, and $\psi = 0$, a Fourier mode satisfies

$$\tau_\ell s^2 + s + D_B^{(\ell)} k^2 = 0. \tag{60}$$

The roots have nonpositive real parts, and the high-wavenumber characteristic speed is

$$v_{\mathrm{char}} = \sqrt{D_B^{(\ell)}/\tau_\ell}. \tag{61}$$

The implementation must enforce $v_{\mathrm{char}} < c$, and in nonrelativistic zooms the stricter practical requirement is $v_{\mathrm{char}} \lesssim \max(c_s, \sigma_\ell)$.

10 Black-hole feeding and observables

The mechanism affects black-hole growth only by changing gas supply. The baryon budget is unchanged,

$$M_{\mathrm{gas}} + M_\star + M_{\mathrm{BH}} + M_{\mathrm{out}} \le f_b M_h. \tag{62}$$

The black-hole mass follows the usual accretion history,

$$M_{\rm BH}(t) = M_0 \exp\left[\frac{1-\epsilon_r}{\epsilon_r}\frac{1}{t_{\rm Edd}}\int^t f_{\rm Edd}(t')\,{\rm d}t'\right], \tag{63}$$

where $f_{\rm Edd}$ is limited by gas supply and feedback. A supply diagnostic is

$$I_{\rm feed} = \int {\rm d}t\, f_{\rm lowJ}(t)\frac{M_{\rm gas}(<R,t)}{t_{\rm dyn}(R,t)}F_{\rm cool}(t)F_{\rm fb}(t). \tag{64}$$

Copy-time transport is relevant only if paired simulations show a statistically significant increase in $I_{\rm feed}$ without violating the speed, conservation and convergence tests.

The observable vector for comparison is generated by forward modelling from the simulated state:

$$\mathbf{y} = (M_{\rm UV}, \beta_{\rm UV}, R_e, M_\star, M_{\rm gas}, N_H, L_X, {\rm FWHM_{BLR}}, M_{\rm BH}, z). \tag{65}$$

A model prediction after selection is

$$P(\mathbf{y}\mid S,\mathcal{M}) = \frac{\int P(S\mid\mathbf{y})P(\mathbf{y}\mid\theta,\mathcal{M})P(\theta\mid\mathcal{M})\,{\rm d}\theta}{\int P(S\mid\mathbf{y})P(\mathbf{y}\mid\theta,\mathcal{M})P(\theta\mid\mathcal{M})\,{\rm d}\theta\,{\rm d}\mathbf{y}}. \tag{66}$$

The same $P(S\mid\mathbf{y})$ is applied to baseline and copy-time simulations, so that differences in compact-source abundance are attributable to dynamics rather than selection.

Table 3: Observable construction for a publication-level test.

Observable	Direct construction	Critical control
$M_{\rm UV}, \beta_{\rm UV}$	stellar population synthesis plus dust/radiative-transfer postprocessing	same IMF, dust, age and attenuation model
R_e	half-light radius in mock images	same PSF and surface-brightness limit
$M_\star, M_{\rm gas}$	simulation truth plus SED-inference emulator	same aperture and inference prior
N_H, L_X	column through gas and obscured AGN spectral model	same orientation sampling and X-ray response
${\rm FWHM_{BLR}}$, $M_{\rm BH}$	sink mass plus virial BLR emulator	same seed and accretion prescription
z	snapshot and lightcone construction	same survey volume and redshift window

11 Halo catalogues, feeding histories and forward-modelled observables

The validation object is a paired catalogue rather than a single high-redshift image. For every initial condition one constructs two rows at each snapshot, baseline and copy-time, with common halo identity, merger history and numerical controls. The minimum halo catalogue is

$$\mathcal{C}_h = \{z, M_h, R_{\rm vir}, \lambda_{\rm B}, j_h, j_{\rm gas}, f_{\rm lowJ}, k_h/k_{\rm peak}, D_B^{(\ell)}, L_\psi, t_{\rm dyn}, t_{\rm drift}, v_{\rm CT}, \sigma_\ell\}. \tag{67}$$

Here

$$j_h = \frac{|\mathbf{J}_h|}{M_h}, \qquad \lambda_{\rm B} = \frac{J_h}{\sqrt{2} M_h V_{\rm vir} R_{\rm vir}}, \tag{68}$$

and the low-angular-momentum fraction is measured directly from cold gas cells or particles,

$$f_{\rm lowJ}(R, j_c) = \frac{\sum_{i \in R,\, T_i < T_c} m_i \, \Theta(j_c - |\mathbf{r}_i \times \mathbf{v}_i|)}{\sum_{i \in R,\, T_i < T_c} m_i}. \tag{69}$$

The threshold j_c is fixed before comparing models; it may be defined by the circular angular momentum at the black-hole feeding aperture, by a fixed percentile of the initial gas distribution, or by the angular momentum required to reach a specified nuclear radius. It is not refitted after seeing the compactness of the final galaxy.

The black-hole feeding history is stored as a time series,

$$\mathcal{C}_{\rm BH} = \{t, z, M_{\rm BH}, \dot{M}_{\rm supply}, \dot{M}_{\rm BH}, f_{\rm Edd}, M_{\rm gas}(< 10{\rm pc}), M_{\rm gas}(< 100{\rm pc}), N_H\}. \tag{70}$$

The distinction between $\dot{M}_{\rm supply}$ and $\dot{M}_{\rm BH}$ is essential: copy-time transport is a supply mechanism and must not be counted as a change to the Eddington limit or to the radiative efficiency. The supply rate is measured through a fixed physical aperture or through a fixed fraction of the virial radius, and the sink rate is then computed by the same accretion and feedback prescription in both simulations.

The forward-modelled catalogue is

$$\mathcal{C}_y = \{M_{\rm UV}, \beta_{\rm UV}, R_e, M_\star, M_{\rm gas}, N_H, L_X, mFWHM_{\rm BLR}, M_{\rm BH}, z, P(S|\mathbf{y})\}. \tag{71}$$

It is generated for each orientation and camera model using the same stellar population synthesis, dust attenuation, point-spread function, surface-brightness threshold, X-ray absorption model and broad-line emulator. The same selection probability $P(S|\mathbf{y})$ is applied to both members of each pair. The comparison statistic is therefore the selected distribution

$$\Delta\langle g \rangle_S = \frac{\sum_i w_i^{\rm CT} g(\mathbf{y}_i^{\rm CT})}{\sum_i w_i^{\rm CT}} - \frac{\sum_i w_i^0 g(\mathbf{y}_i^0)}{\sum_i w_i^0}, \qquad w_i = P(S|\mathbf{y}_i), \tag{72}$$

with paired bootstrap or hierarchical modelling over initial conditions. A detection claim requires a coherent sign pattern: increased central gas supply, larger selected obscured fraction or X-ray active fraction where allowed by absorption, smaller selected R_e, and a finite-band turnover with j_h or $k_h/k_{\rm peak}$. A change in only one observable is not sufficient.

12 Predictions and discriminants

The model makes several nontrivial predictions.

First, molecular transport is negligible on 10–100 pc scales. An implementation in which the molecular coefficient alone drives compaction would indicate numerical overdiffusion rather than the filtered transport channel derived here.

Second, the source must satisfy the power window (43). The channel fails if $D_B^{(\ell)}$ measured from velocity autocorrelations is below $LL_\psi/t_{\rm dyn}$, or if the required drift speed exceeds $\max(c_s, \sigma_\ell)$.

Third, because the receiver window is finite-band, the compaction excess should be nonmonotonic in angular-structure proxies. A purely low-spin inflow model tends to predict a monotonic increase

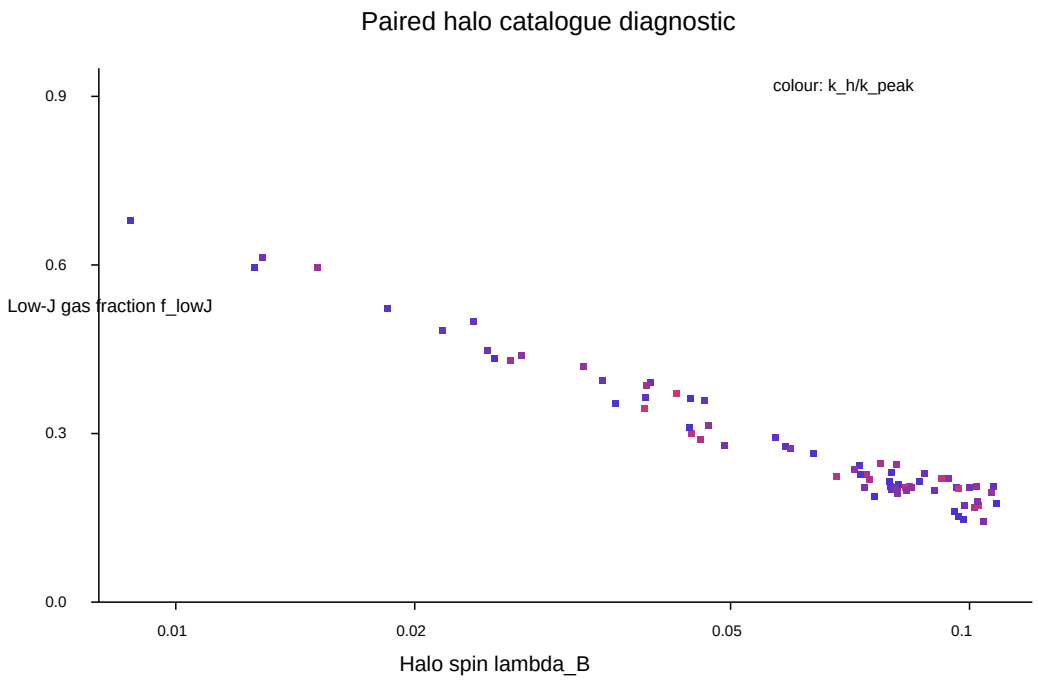

Figure 6: Catalogue-level diagnostic for the halo spin and low-angular-momentum gas fraction. The distributed table schema records j_h, f_{lowJ}, the receiver-band coordinate and the power-window quantities for each matched halo. The shown points are a deterministic smoke test of the data contract, not production cosmological evidence.

toward low angular momentum; the copy-time excess peaks when low-angular-momentum gas and receiver band-pass overlap:

$$\Delta_{\mathrm{CT}}(j_h) \propto f_{\mathrm{lowJ}}(j_h) \frac{(k_h/k_{\mathrm{peak}})^2}{[1+(k_h/k_{\mathrm{peak}})^2]^2}, \tag{73}$$

where k_{peak} is fixed by Eq. (51).

Fourth, copy-time runs should show a sequence rather than a single static signature: central gas concentration rises; columns N_H increase; black-hole feeding increases only if feedback does not evacuate the reservoir; subsequent radiation or stellar feedback may clear dust and produce a blue compact phase. This is compatible with the existence of both obscured red sources and luminous blue high-redshift systems, but only a forward-modelled paired run can decide whether the mechanism improves the distribution.

Fifth, the selection-corrected distribution $P(\mathbf{y} \mid S)$ is constrained jointly by compactness, gas column, black-hole mass or luminosity, and abundance. A change confined to R_e at the expense of luminosity functions, metallicities or X-ray constraints would be observationally disfavoured.

13 Numerical validation protocol

A quantitative claim of cosmological impact requires matched radiation-hydrodynamic zoom simulations. The following protocol specifies the validation standard used to convert the transport construction into a numerical prediction.

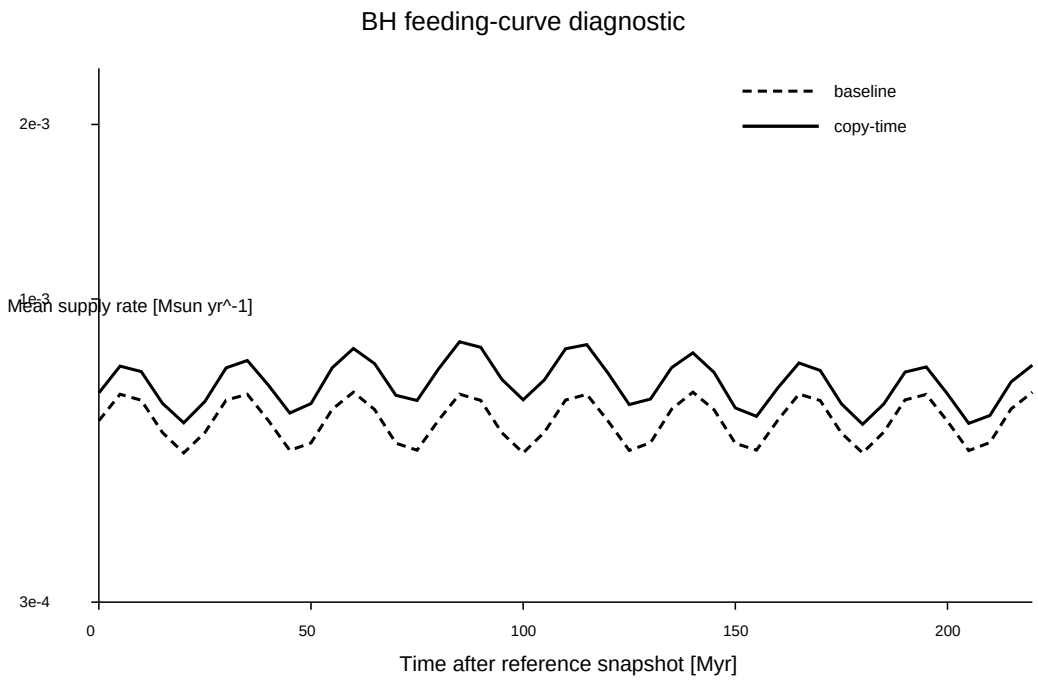

Figure 7: Black-hole feeding-history diagnostic. The required production observable is not only the final black-hole mass but the paired time series of central gas supply, sink accretion, obscuring column and Eddington ratio. The plotted curves are a smoke test of the storage and plotting pipeline.

1. Select halos by initial conditions and halo catalogues, not by high-redshift compactness after the fact.
2. Run paired baseline and copy-time simulations with identical cosmology, phases, mass resolution, force resolution, chemistry, cooling, radiative transfer, stellar feedback, metal enrichment and black-hole sink rules.
3. At each hydrodynamic step compute R_r, $A_{2,r}$, $\dot{\mathcal{I}}^{\parallel}$, $\dot{\mathcal{I}}^{\perp}$, ψ, $D_B^{(\ell)}$ and τ_ℓ from the local state.
4. Insert $\mathbf{J}_{\mathrm{CT}}$ only as a conservative face flux and advect the corresponding momentum and enthalpy.
5. Recompute self-gravity after the density update using Eq. (59).
6. Apply identical nonequilibrium cooling, chemistry, star formation, feedback and black-hole accretion modules after the conservative update.
7. Perform convergence in gas mass, force softening or AMR level, photon angular resolution, photon groups, chemistry time step, CT subcycling and sink radius.
8. Generate mock JWST, Chandra and XMM observables and apply the same selection function to both model families.

14 Code and reproducibility

The accompanying code regenerates the figures and CSV diagnostics. The diagnostics evaluate: (i) the molecular null result; (ii) the filtered-mobility power criterion; (iii) the projected channel coefficients for A_2; (iv) a finite-band receiver window; and (v) a nonmonotonic angular-structure

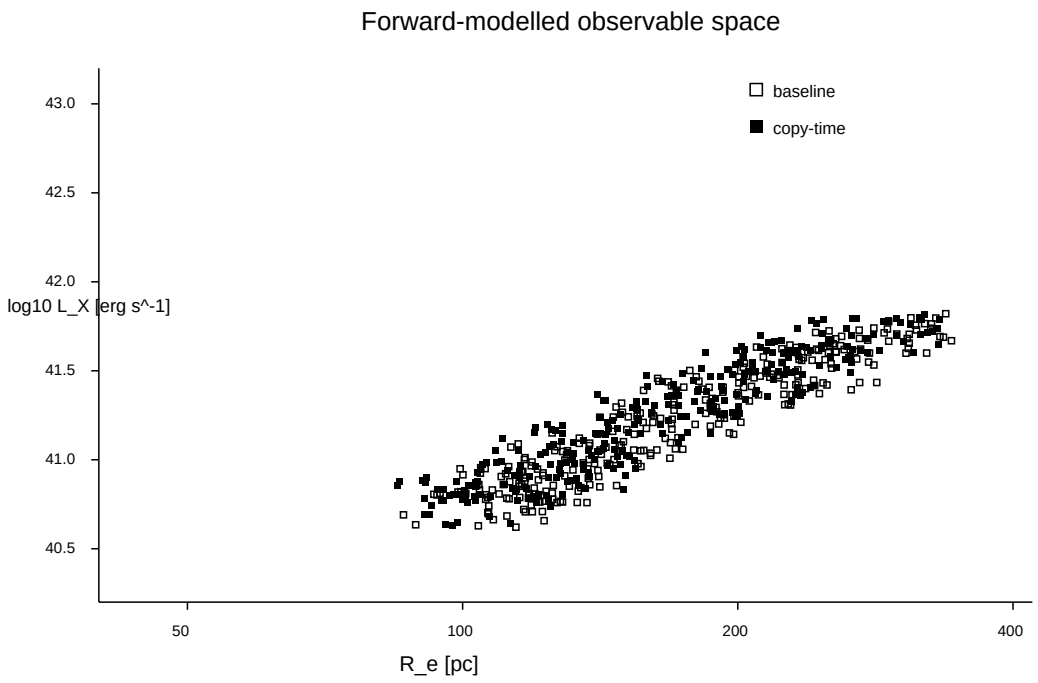

Figure 8: Forward-modelled observable-space diagnostic. Baseline and copy-time runs must be mapped to the same JWST and X-ray observable vector and weighted by the same selection function. The displayed catalogue is synthetic and serves only to verify the comparison machinery.

discriminant. Their scope is algebraic and dimensional; cosmological inference requires the matched simulations and selection modelling defined in Sec. 12.

15 Conclusion

This work formulates copy-time transport as a projected Onsager mechanism derived from microphysical records after the standard RHD response is removed. The structural Fisher scalar is dimensionless; the quadratic amplitude A_2 follows channel by channel from projected Poisson record rates; the Radon-Nikodym measure yields the thermodynamic force; and Onsager theory fixes $L^{(\ell)}_{B\psi} = q_Q n_b D^{(\ell)}_B$. Molecular diffusion is excluded as the galaxy-scale channel by dimensional analysis. Dynamical relevance requires a filtered mobility and a structural Fisher gradient satisfying the power inequalities. The RHD insertion is conservative, entropy-producing and hyperbolic, and the primary linear CMB/BAO source vanishes under the projection hypotheses. The resulting predictions are testable through paired zoom simulations, halo catalogues containing j_h and $f_{\rm lowJ}$, black-hole supply histories and selection-corrected JWST/X-ray forward modelling; the distributed catalogue schemas specify the required data products for that test.

References

[1] L. Onsager, Reciprocal relations in irreversible processes I, *Phys. Rev.* **37**, 405 (1931).

[2] L. Onsager, Reciprocal relations in irreversible processes II, *Phys. Rev.* **38**, 2265 (1931).

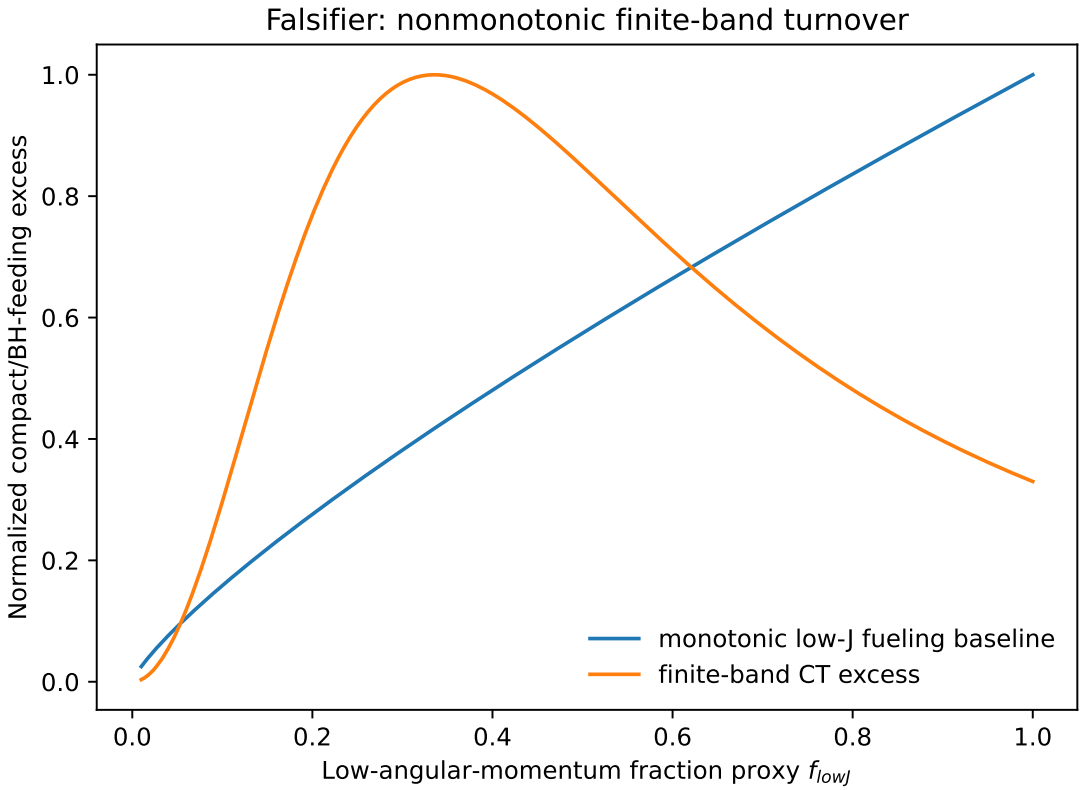

Figure 9: Qualitative discriminant. Standard low-angular-momentum feeding generally produces a monotonic trend, while the screened receiver mechanism predicts a finite-band turnover. The prediction must be tested in halo catalogues with measured spin, f_{lowJ}, gas concentration and black-hole feeding histories.

[3] M. S. Green, Markoff random processes and the statistical mechanics of time-dependent phenomena II, *J. Chem. Phys.* **22**, 398 (1954).

[4] R. Kubo, Statistical-mechanical theory of irreversible processes I, *J. Phys. Soc. Jpn.* **12**, 570 (1957).

[5] H. Mori, Transport, collective motion, and Brownian motion, *Prog. Theor. Phys.* **33**, 423 (1965).

[6] R. Zwanzig, Memory effects in irreversible thermodynamics, *Phys. Rev.* **124**, 983 (1961).

[7] S. R. de Groot and P. Mazur, *Non-Equilibrium Thermodynamics* (North-Holland, Amsterdam, 1962).

[8] S. Chapman and T. G. Cowling, *The Mathematical Theory of Non-Uniform Gases*, 3rd ed. (Cambridge University Press, Cambridge, 1970).

[9] L. Spitzer, *Physics of Fully Ionized Gases*, 2nd ed. (Interscience, New York, 1962).

[10] W. Israel and J. M. Stewart, Transient relativistic thermodynamics and kinetic theory, *Ann. Phys.* **118**, 341 (1979).

Table 4: Minimum convergence tests. These tests are required for a numerical assessment of the transport operator.

Test	Required variation	Failure mode detected
Mass resolution	at least 8-fold gas-particle/cell mass change	numerical diffusion and unresolved cl
Force resolution	softening or AMR level sweep	artificial central concentration
Photon angular resolution	ray or moment closure change	spurious receiver anisotropy
Photon groups	UV/ionizing/X-ray group sweep	wrong A_2 channel weights
Chemistry step	subcycling tolerance sweep	fake cooling-triggered inflow
CT timestep	hyperbolic CFL sweep	unstable transport current
Sink/accretion radius	radius sweep	artificial BH supply

[11] G. S. Denicol et al., Derivation of transient relativistic fluid dynamics from the Boltzmann equation, *Phys. Rev. D* **85**, 114047 (2012).

[12] Planck Collaboration, Planck 2018 results VI. Cosmological parameters, *Astron. Astrophys.* **641**, A6 (2020).

[13] D. Blas, J. Lesgourgues and T. Tram, The Cosmic Linear Anisotropy Solving System II, *JCAP* **2011**, 034 (2011).

[14] A. Lewis, A. Challinor and A. Lasenby, Efficient computation of CMB anisotropies, *Astrophys. J.* **538**, 473 (2000).

[15] J. Torrado and A. Lewis, Cobaya: code for Bayesian analysis of hierarchical physical models, *JCAP* **2021**, 057 (2021).

[16] S. Carniani et al., Spectroscopic confirmation of two luminous galaxies at a redshift of 14, *Nature* **633**, 318 (2024).

[17] A. Ferrara, The eventful life of GS-z14-0, the most distant galaxy at redshift $z = 14.32$, *Astron. Astrophys.* **689**, A310 (2024).

[18] A. Bogdan et al., Evidence for heavy-seed origin of early supermassive black holes from a $z \approx 10$ X-ray quasar, *Nat. Astron.* **8**, 126 (2024).

[19] A. J. Taylor et al., CAPERS-LRD-z9: A gas-enshrouded little red dot hosting a broad-line active galactic nucleus at $z = 9.288$, *Astrophys. J. Lett.* **989**, L7 (2025).

[20] E. Banados et al., An 800-million-solar-mass black hole in a significantly neutral Universe at redshift 7.5, *Nature* **553**, 473 (2018).

[21] K. Inayoshi, E. Visbal and Z. Haiman, The assembly of the first massive black holes, *Annu. Rev. Astron. Astrophys.* **58**, 27 (2020).

[22] M. Volonteri, M. Habouzit and M. Colpi, The origins of massive black holes, *Nat. Rev. Phys.* **3**, 732 (2021).

[23] R. Teyssier, Cosmological hydrodynamics with adaptive mesh refinement: a new high-resolution code called RAMSES, *Astron. Astrophys.* **385**, 337 (2002).

[24] G. L. Bryan et al., ENZO: an adaptive mesh refinement code for astrophysics, *Astrophys. J. Suppl.* **211**, 19 (2014).

[25] V. Springel, E pur si muove: Galilean-invariant cosmological hydrodynamical simulations on a moving mesh, *MNRAS* **401**, 791 (2010).

[26] P. F. Hopkins, A new class of accurate, mesh-free hydrodynamic simulation methods, *MNRAS* **450**, 53 (2015).

[27] B. D. Smith et al., GRACKLE: a chemistry and cooling library for astrophysics, *MNRAS* **466**, 2217 (2017).